

# Growth and Characterization of Bis(thiourea) Antimony Tribromide: A Reliable Non-Linear Optical Crystal

N. R. Rajagopalan<sup>1,2</sup> · P. Krishnamoorthy<sup>3</sup>

Received: 5 October 2016 / Accepted: 18 November 2016 / Published online: 22 November 2016  
© Springer Science+Business Media New York 2016

**Abstract** Bis(thiourea) antimony tribromide (BTAB) single crystals of semi organic non-linear optical (NLO) crystal category have been effectively grown and harvested by the technique of slow solvent evaporation. The important nucleation kinetic parameter values have been deduced for the title crystal and the agreement between the experimental and theoretical values of interfacial surface energy has been established. The orthorhombic structure and  $Cmc_2_1$  space group have been identified with the aid of single crystal X-ray diffraction studies. To validate the stoichiometry and the purity of the crystals, elemental analysis has been carried out. The UV transmittance spectrum has been employed to deduce the significant optical constant and oscillator parameter values. In the region of absorption edge, Urbach tail energy has been determined to ascertain the crystalline perfection of BTAB. The etching studies inferred the step growth pattern of the crystal. The phase matchable SHG efficiency of BTAB has been tested by Kurtz–Perry technique. The negative photoconductivity and low birefringence values have been revealed by photoconductivity study and birefringence study respectively. Dielectric and ac conductivity studies have helped in calculating the activation energy values of the electrical process. Important solid state parameters such as valence electron plasma energy, Penn gap, Fermi energy and polarisability

have been calculated for the BTAB crystal. To assess the mechanical stability of the crystal Vicker's micro hardness analysis has been performed and important mechanical parameters have been elucidated.

**Keywords** NLO · SHG · Nucleation kinetics · Solid state parameters · Optical constants · Hardness · Negative photoconductivity

## 1 Introduction

The momentous growth in the domain of non-linear optics (NLO) has been consistently facilitated by the advent of high intensity lasers and the advances in crystal technology. The further progress in this NLO field will be dictated by the availability of newer and better device fabricating materials. In the current era of technology, the contribution of NLO crystals in the emerging fields of laser technology, optical signal processing, photonic technology and optical communication has been widely acknowledged and highly appreciated by the engineering and scientific community [1]. In the ardent quest for newer NLO materials, inorganic materials stand a thin chance due to their inherent limitation on the maximum attainable non-linearity. On the other hand, the difficulties encountered in growing device grade single crystals of organic origins drove the researchers towards a new class of materials known as semi-organics [2]. The semi-organic materials are at the forefront of NLO field as a tribute to their potential in combining the advantages of organic and inorganic materials which include low angular sensitivity, chemical flexibility, higher order of non-linear susceptibility, enhanced mechanical robustness, thermal stability, wide transparency range and high laser damage threshold [3]. As a result, growth and characterization

✉ P. Krishnamoorthy  
kristhiresearch@gmail.com

<sup>1</sup> Research and Development Centre, Bharathiar University, Coimbatore 641046, India

<sup>2</sup> Department of Chemistry, St. Joseph's College of Engineering, Chennai 600119, India

<sup>3</sup> Department of Chemistry, Dr. Ambedkar Govt. Arts College, Chennai 600039, India

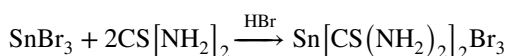
of semi organic crystals has become a subject of perpetual concern to enable them to be utilized prolifically in NLO device fabrication. Among the semi-organic NLO materials, metal complexes of thiourea have attracted considerable attention of researchers because the centrosymmetric thiourea molecule becomes non-centrosymmetric on metal coordination which is an essential prerequisite for a crystal to exhibit non-linear optical activity [4]. The synthesis and systematic characterization of certain well known thiourea based semi-organic NLO materials have been reported in literature which include tris(thiourea) zinc selenate [5], bis(thiourea) zinc acetate [6], bis(thiourea) lead chloride [7], bis(thiourea) zinc chloride [8] and bis(thiourea) strontium chloride [9]. In this regard, an attempt has been made to grow and characterize bis(thiourea) antimony tribromide (BTAB-for convenient notation) single crystals, for which only limited characterization details are available in literature [10].

In the crystal growth regime, characterization of a material has a pivotal role as the growth itself. The aim of the present research work is to grow and characterize high quality BTAB single crystals. In a broader spectrum, the focus will be on evaluating the growth parameters and analyzing the physico chemical properties of BTAB crystals. The etching studies and elemental analysis have been carried out as a part of this present study. Further investigations on the optical properties of the BTAB crystal have also been carried out and the findings related to the optical constants and oscillator parameters have been reported. The second harmonic generation (SHG) and phase matching nature of the title crystal have been tested and the inferences have been discussed. The photoconductivity nature and birefringence patterns of the crystals have been analysed. An extensive study on the mechanical parameters of the crystal has been carried out. A detailed study on the electrical behaviour and solid state parameters of BTAB has been done and the results have been further correlated with its NLO device fabrication suitability.

## 2 Material and Methods

### 2.1 Synthesis, Meta Stable Zone Width and Induction Period Measurements of BTAB

The synthesis of BTAB has been performed by taking analytical grade thiourea and antimony tribromide in the ratio of 2:1, as per the following chemical reaction.



HBr is added to the reaction mixture to provide an acidic environment (pH=5.1) to avoid the antimony

trioxide formation which will hinder the crystal formation. To avoid co-precipitation of multiple phases, the solution was thoroughly stirred using a magnetic stirrer. Recrystallisation method has been adopted to enhance the purity of the product. For the selection of optimum temperature and suitable solvent for any crystal growth mechanism, conducting a solubility test is always preferred. Moreover the crystal size is primarily dictated by the amount of the sample present in the solution and its solubility in the available solvent. The solubility study has been done by taking water as the solvent and the synthesized BTAB as the solute. A constant stirring of the resultant solution has been continued using a motorized stirrer at 303 K in a constant temperature bath controlled to  $\pm 0.1^\circ\text{C}$  accuracy. After the point of super-saturation, the equilibrium concentration of the solute has been analyzed gravimetrically, in which a sample of the clear supernatant liquid has been pipetted out and a weighed quantity of the sample has been analyzed for the solute content. The procedure has been repeated for other temperatures (308, 313, 318 and 323 K) also and the results have been recorded. By making use of the solubility test, the saturation solutions of BTAB have been prepared. By following the concepts of conventional poly-thermal method [11], the saturated solution has been cooled from the preheated temperature and the first visible critical nucleus formation temperature has been noted down. This is taken as the nucleation temperature of the crystal. The meta stable zone width value has been deduced from the difference between the nucleation temperature and saturation temperature. For growing good quality crystals, higher meta stable width is preferred. The solubility and nucleation curves are shown in Fig. 1a. The solubility curve exhibits a positive gradient. The isothermal

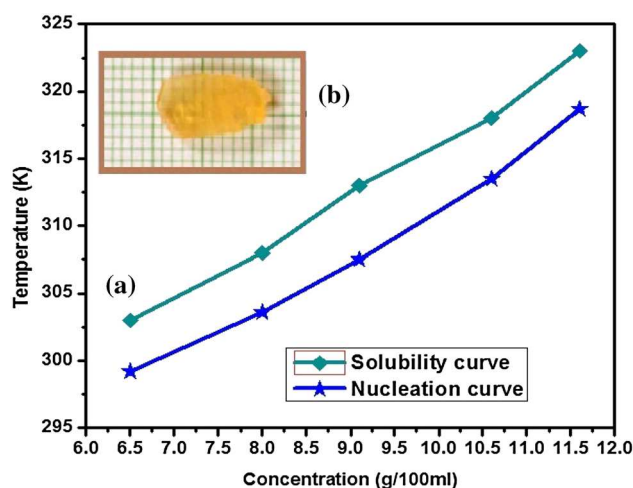


**Fig. 1** a Solubility and nucleation curves of bis(thiourea) antimony tribromide. b As grown crystal of bis(thiourea) antimony tribromide

method [12] defines the induction period as the time taken for critical nuclei formation at a specific temperature. Hence, to modify and control the nucleation rate of any crystal, knowledge of the induction period will be of vital importance. For all the five temperatures (303, 308, 313, 318 and 323 K) the values of induction period have been measured by isothermal method and experiments were done repeatedly to ascertain the correctness of the observed induction period values.

## 2.2 Crystal Growth

BTAB crystals have been grown from the saturated solution by slow evaporation method. Using Whatman filter paper, the solution has been filtered thoroughly into a clean glass beaker. The solution in the beaker was covered tightly with a perforated polythene sheet to restrict the fast evaporation and kept undisturbed in a dust free environment. Crystallisation took place within 33–35 days. When the crystals attained suitable size and shape, good quality yellow coloured BTAB crystals have been harvested. Figure 1b shows the photograph of the grown crystal BTAB.

## 2.3 Characterization

Enraf (Bruker) Norius CAD4 diffractometer with Mo K $\alpha$  ( $\lambda=0.7170$  Å) has been employed for single crystal X-ray diffraction analysis. Elemental analysis was achieved by Perkin–Elmer series-II-2400 CHNS/O elemental analyser. Magnus MLX optical microscope in the reflective mode was the tool utilized for etching studies of BTAB crystals. The UV–Vis spectrum of the crystal was obtained from Shimadzu UV-106 spectrometer in the region of 180–800 nm. Mechanical analysis was done with the aid of Leitz–Wetzler hardness tester. Quanta ray spectra physics Nd:YAG laser has been employed in the studies on phase matching SHG by Kurtz method. The results of dielectric studies in the frequency range of 50 Hz–5 MHz have been obtained by Hiocoki model 3532-50 LCR Hitester instrument. The photoconductivity studies on the crystal have been performed by a Keithley 480 picoammeter. The birefringence studies were done by Modified Channel Spectrum methodology using He–Ne laser source.

## 3 Results and Discussion

### 3.1 X-ray Diffraction Studies

X-ray diffraction study is the reliable and widely used technique to ascertain the lattice parameters and provide valuable information regarding the structural details of a grown crystal. The results of single crystal X-ray diffraction

study on BTAB pointed out the values of its axial cell lengths as  $a=12.269$  Å,  $b=11.671$  Å,  $c=18.620$  Å and  $v=2666.225$  (Å)<sup>3</sup>. The interfacial angles have been found to be  $\alpha=\beta=\gamma=90^\circ$ . The XRD results suggested that the BTAB crystal belongs to orthorhombic system and Cmc2<sub>1</sub> space group. The observed values have been found to be consistent with the reported literature values [10].

### 3.2 Nucleation Kinetics

The nucleation kinetics study will provide idea on crucial parameters for getting good quality crystals. An extensive knowledge of super saturation, controlled nucleation rate and optimal crystal growth parameters can be obtained from the nucleation study. Another interesting aspect of this nucleation studies is that it can also be used to test the validity of various nucleation theories.

#### 3.2.1 Critical Nucleation Parameters

The interracial surface energy prevailing between the crystal and the surrounding saturated solution can be considered as a pivotal factor in determining the rate of nucleation and crystal growth [13]. The classical theory of homogeneous spherical nucleus formation [14] points out a relationship between the induction period ( $\tau$ ) and interfacial surface energy ( $\gamma$ ) as

$$\ln \tau = -\ln B + [16\pi\gamma^3V^2N_A/3R^3T^3(\ln S)^2] \quad (1)$$

where B is constant, V is molar volume,  $N_A$  is Avogadro number, R is gas constant and S is the ratio between the mole fractions of solute in the super saturated (C) and saturated ( $C_0$ ) solution at temperature (T) which is known as super saturation ratio. Since  $\ln B$  weakly depends on temperature, the experimental values of interfacial surface energy can be calculated from the modified version Eq. (1) as,

$$\gamma = [3R^3T^3(\ln S)^2 \ln \tau / 16\pi V^2 N_A]^{1/3} \quad (2)$$

The crystallization process is also depending on the Gibbs free energy change ( $\Delta G$ ) between the crystal and solution. The expression for this free energy change is rendered by homogeneous spherical nucleation theory [15] as,

$$\Delta G = 4\pi r^2\gamma + (4/3)\pi r^3\Delta G_v \quad (3)$$

where  $r$ =radius of the nucleus and  $\Delta G_v$ , a negative quantity, is the energy change per unit volume. The chemical potential difference between the crystal and its mother liquor is testified by the first term and the new surface formation is signaled by the second term. According to classical nucleation theory, as the nucleus grows in size,

$\Delta G$  increases, reaches a maximum value and then starts decreasing. The nucleus size which corresponds to maximum  $\Delta G$  value is known as critical nucleus. At this critical state, the radius of the critical nucleus ( $r^*$ ) is given by

$$r^* = -2\gamma/\Delta G_v \tag{4}$$

where  $\Delta G_v = -(kT \ln S)/v$  ( $v$  is the specific volume of the solute).

The number of molecules in the critical nucleus is known as critical number ( $i^*$ ), is given by

$$i^* = 4\pi(r^*)^3/3v \tag{5}$$

The expression to deduce the value of Gibbs free energy change for the formation of the critical nucleus (critical free energy barrier,  $\Delta G^*$ ) is

$$\Delta G^* = 16\gamma^3V^3/3k^2T^2(\ln S)^2 \tag{6}$$

The number of critical nuclei formed per unit time per unit volume can be considered as the rate of nucleation ( $J$ ), which can be calculated from the expression,

$$J = A \exp(-\Delta G^*/kT) \tag{7}$$

where  $A$  is constant whose value is  $10^{30}$ . By substituting the corresponding values in Eqs. (2–7), the experimental

values of interfacial surface energy, free energy change, radius of critical nucleus, critical number, critical free energy barrier and rate of nucleation have been arrived at and tabulated in Table 1.

### 3.2.2 Validation of Modern Nucleation Theory Models

Various modern nucleation theories suggested the different models and expression for calculating the interfacial surface energy. For validation purpose, we have chosen three such theories. As per Bennema [16] model,

$$\gamma = (kT/a^2)[0.173 - 0.248 \ln(X_m)] \tag{8}$$

where  $T$  is the temperature in Kelvin,  $k$  is the Boltzmann's constant,  $X_m$  is the mole fraction of the solute and  $a=6V/\pi$ , where  $V$  is the molar volume.

In the view of Christoffersen et al. [17],

$$\gamma = 0.282 \times (kT/d^2) \times \ln(C/C_0) \tag{9}$$

where  $d$  is the mean diameter of ions.

While Nielson and Sohnel [18] model concluded,

$$\gamma = (kT/hd^2) \times \ln(C/C_0) \tag{10}$$

**Table 1** Nucleation parameters of BTAB crystals

Saturation temp. (K)	Nucleation temp. (K)	Meta stable zone width	Super saturation ratio (C/C <sub>0</sub> )	Free energy change ( $\Delta G_v$ ) ( $\times 10^6$ ) (J/m <sup>3</sup> )	Critical free energy ( $\Delta G_c$ ) ( $\times 10^{-20}$ ) (J)	Critical radius ( $r^*$ ) (nm)	Critical number ( $i^*$ )	Nucleation rate (J) ( $\times 10^{27}$ ) (nuclei/s/vol)
303	299.2	3.8	1.2	-2.287	2.413	1.714	63.303	3.117
			1.3	-3.292	2.319	1.499	42.282	3.901
			1.4	-4.221	2.230	1.361	31.699	4.830
			1.5	-5.087	2.176	1.269	25.667	5.497
308	303.6	4.4	1.2	-2.325	2.447	1.713	63.164	3.157
			1.3	-3.346	2.347	1.496	42.099	3.995
			1.4	-4.291	2.248	1.358	31.434	5.050
			1.5	-5.171	2.195	1.266	25.472	5.719
313	307.5	5.5	1.2	-2.363	2.477	1.711	62.917	3.229
			1.3	-3.400	2.375	1.494	41.914	4.094
			1.4	-4.361	2.266	1.354	31.187	5.264
			1.5	-5.255	2.213	1.262	25.269	5.959
318	313.5	4.5	1.2	-2.401	2.505	1.708	62.629	3.315
			1.3	-3.455	2.404	1.492	41.755	4.180
			1.4	-4.430	2.286	1.351	30.963	5.467
			1.5	-5.339	2.229	1.259	25.058	6.220
323	318.7	4.3	1.2	-2.438	2.536	1.706	62.407	3.383
			1.3	-3.509	2.426	1.489	41.49	4.325
			1.4	-4.500	2.297	1.346	30.626	5.785
			1.5	-5.423	2.227	1.252	24.639	6.770

**Table 2** Values of inter facial surface energy ( $\gamma$ ) for BTAB crystals ( $\text{mJ/m}^2$ )

Saturation temperature (K)	Experimental value	Christof-fersen model	Nielson–Sohnel model	Bennema model
303	2.632	2.378	2.479	2.826
308	2.670	2.417	2.521	2.873
313	2.708	2.456	2.562	2.919
318	2.745	2.495	2.603	2.966
323	2.779	2.535	2.644	3.012

**Table 3** Elemental analysis of BTAB

Elements	C	H	N	S
Experimental value %	4.59	1.52	10.86	12.54
Calculated value %	4.68	1.57	10.91	12.48

where  $h$  is the hydration number varying from 3.4 to 5.

The interfacial surface energy values that have been calculated experimentally have been proved to be in good agreement with the values deduced from the Eqs. (8–10) and are presented in Table 2. It has been learnt from the Tables 1 and 2 that the super saturation and temperature share an inverse relationship with free energy change, critical radius and critical number. Anyhow with increasing temperature and super saturation, interfacial surface energy and nucleation rate were increasing. The data in Table 2 provide us with the proof of the agreement between the experimental and theoretical values of interfacial surface energy values. Hence we can state that the evaluated nucleation parameters obtained in the present study facilitate the optimal growth of BTAB crystals.

### 3.3 Elemental Analysis

A great deal of information regarding the purity and the stoichiometry of the sample can be furnished by the elemental analysis. BTAB crystal has been subjected to elemental analysis for its carbon, hydrogen, nitrogen and sulphur content which established the stoichiometry of the crystal  $\text{Sb}[\text{CS}(\text{NH}_2)_2]_2\text{Br}_3$ . Table 3 shows that the experimental and calculated values of C, H, N and S present in the sample are in concordance with each other. This trend actually recognizes the purity of the BTAB crystal. Rhodamine B spot test [19] has been performed to check the presence of antimony in the sample and the same has been inferred by the resultant violet coloration.

### 3.4 Ultra Violet Spectral Analysis

Presently, the optical properties of NLO materials are the subject of keen interest, in response to the increasing demand for optoelectronic devices that may function successfully at the processing wavelengths. The UV–Vis transmittance analysis plays an important role in identifying the potential of a NLO crystal because any crystal can be of practical applicability only if it shows a wide transparency window without any absorption at the fundamental and second harmonic wavelengths [20]. From the UV transmittance spectrum (Fig. 2a) of the BTAB crystal, one may notice that the lower cutoff region has been obtained at 249 nm and a steady transmittance of 85% has been exhibited in the visible region. These values enumerate the crystal's prominence for laser frequency doubling and photonic applications in UV and visible region. The  $\pi$  orbital electron delocalization caused by the mesomeric effect of thiourea complex is responsible for its NLO behaviour and high absorbance (low transmittance) in the UV region below its cutoff wavelength [21, 22]. Further, the BTAB crystal proves its usefulness in optical harmonic generation related applications with its wide transparency window. Theoretically, the band gap ( $E_g$ ) can be obtained by using the expression.

$$E_g = h \times (c/\lambda) \quad (11)$$

where  $h$  is Planck's constant,  $c$  is the velocity of light and  $\lambda$  is the cut-off wavelength. The high band gap value (4.96 eV) calculated from the above equation recognizes the suitability of BTAB for various optoelectronic device fabrications.

An established method, known as Tauc's plot method is a versatile tool to verify the correctness of the band gap calculated theoretically. As per Tauc's relation [23],

$$\alpha h\nu = \beta [h\nu - E_{op}]^m \quad (12)$$

where  $h\nu$  is photon energy,  $E_{op}$  is the optical energy band gap,  $\beta$  is a constant,  $m$  carries values depending on the nature of electronic transitions [24] and  $\alpha$  is the adsorption coefficient such that

$$\alpha = (2.303/t) \times \log(1/T) \quad (13)$$

where  $t$  is the thickness of the crystal. In order to decide the value of  $m$  in Eq. (12) the type of transitions between various energy levels must be predicted. For direct allowed transition and direct forbidden transition, the  $m$  value will be 0.5 and 1.5 respectively. In the case of indirect allowed and indirect forbidden transition, the value of  $m$  becomes 2 and 3 respectively [25].

To know the type of transition, we are considering the differential form of Eq. [12] as,

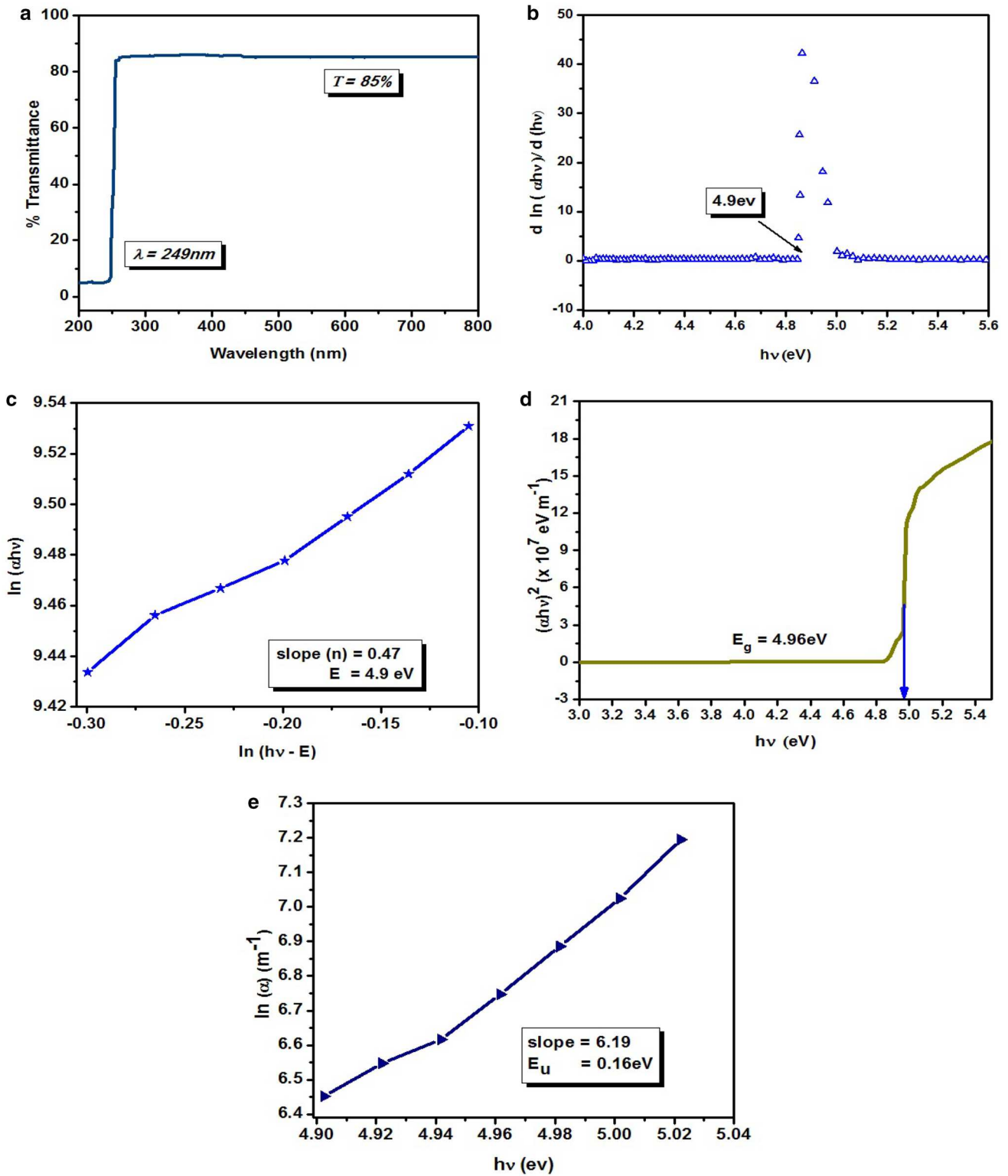


**Fig. 2** **a** UV transmittance spectrum of BTAB. **b** Plot of  $d \ln(\alpha h\nu)/d(h\nu)$  vs.  $h\nu$  for BTAB crystal. **c** Variance of  $\ln(\alpha h\nu)$  with respect to  $\ln(h\nu - E)$  for BTAB. **d** Tauc's plot of BTAB crystal. **e** Urbach's tail plot of BTAB

$$[\text{dln}(\alpha h\nu)/\text{d}(h\nu)] = [m/h\nu - E] \quad (14)$$

On plotting  $[\text{dln}(\alpha h\nu)/\text{d}(h\nu)]$  vs.  $h\nu$  (Fig. 2b), we encountered a distinct discontinuity at a particular value of  $h\nu$  where a most probable optical transition would have occurred with respect to a particular optical band gap [26] whose value was observed as 4.9 eV. A graph of  $\ln(\alpha h\nu)$  vs.  $\ln(h\nu - E)$  was drawn (Fig. 2c) and the resultant points were subjected to linear fitting. The slope (0.47) of the resultant linear fit curve has been taken as the value of  $m$ . The closeness of  $m$  value to 0.5 indicates the occurrence of direct and allowed electronic transitions in BTAB crystals. For direct allowed transitions, the Eq. (12) becomes

$$\alpha h\nu = \beta [h\nu - E_{\text{op}}]^{1/2} \quad (15)$$

The Tauc's plot which is dealing with variance of  $(\alpha h\nu)^2$  with respect to the photon energy has been shown in Fig. 2d. The experimental  $E_g$  value can be obtained by the extrapolation of the linear part of the graph [27].

From the extrapolated line, the band gap energy of BTAB has been determined as 4.96 eV which is in very good agreement with the theoretical  $E_g$  value. As the presence of lattice defects pulls down the band gap value [28], higher  $E_g$  value of BTAB infers that crystal is having minimal defect concentration. The higher value of transmittance showed by BTAB can also be considered as a result of this wide band gap [29]. Urbach relationship [30] is employed to typify the nature of adsorption coefficient in the exponential edge region as,

$$\alpha(h\nu) = \alpha_0 \exp(h\nu/E_u) \quad (16)$$

where  $\alpha_0$  is constant and  $E_u$  is Urbach's energy.

Urbach's energy is calculated by taking inverse of the slope of the plot drawn between  $\ln(\alpha)$  vs.  $h\nu$  (Fig. 2e). Whenever the dislocations, defects and thermal vibrations create tailing of energy states in the energy gap, as a consequence, this Urbach's energy value would be increased. Hence the lower  $E_u$  value is an indicator of high crystallinity. In the case of BTAB, the obtained lower  $E_u$  (0.16 eV) value attested the good crystalline nature of the crystal [31]. The evaluation of crucial optical constants like reflectance, refractive index, optical and electrical conductivities, extinction coefficient and electrical susceptibility serves as a mean of appreciating the usefulness of NLO materials in photonic devices. Reflectance ( $R$ ) is the ratio of the energy of the reflected light to incident light. The refractive index ( $n$ ) is the ratio of the speed of light in vacuum and that of the experimental medium which can be closely related with the symmetry and structure of a crystal. When an electromagnetic radiation falls on a material, the way in which the material respond to the frequency of the incident radiation may be expressed in terms of its optical conductivity ( $\sigma_{\text{op}}$ )

and electrical conductivity ( $\sigma_e$ ). Due to the phenomenon of scattering and absorption, there may loss in the intensity of incident radiation. When it is measured for an unit distance in a medium, it gives the value of extinction coefficient ( $K$ ). These inter related optical constants may be easily deduced by making use of standard formulae reported in literature [32] as,

$$R = \frac{\exp(-\alpha t) \pm \sqrt{\exp(-\alpha t)T - \exp(-3\alpha t)T + \exp(-2\alpha t)T * T}}{\exp(-\alpha t) + \exp(-2 - \alpha t)T} \quad (17)$$

$$n = \left[ -(R + 1) \pm 2\sqrt{R} \right] / [R - 1] \quad (18)$$

$$\sigma_{\text{op}} = \lambda n c / 4\pi \quad (19)$$

$$\sigma_e = 2\lambda \sigma_{\text{op}} / \alpha \quad (20)$$

$$K = \lambda \alpha / 4\pi \quad (21)$$

The values of the real ( $\epsilon_r$ ) and imaginary ( $\epsilon_i$ ) parts of dielectric constant have been deduced as,

$$\epsilon_r = n^2 - K^2 \quad (22)$$

$$\epsilon_i = 2nK \quad (23)$$

Further, the electrical susceptibility ( $\chi$ ) can be deduced as,

$$\chi = [n^2 - K^2 - (\epsilon_r + \epsilon_i)] / 4\pi \quad (24)$$

The dependence of reflectance and refractive index on wavelength is shown in Fig. 3a, b respectively. A normal dispersion behaviour has been observed in the plot where with increasing wavelength the indices of refraction decrease and becomes saturated. From the Fig. 3c, depicting the variance of conductivity with photon energy, one may notice optical conductivity increases with increase in photon energy. The behaviour of extinction coefficient and electrical susceptibility with respect to photon energy has been portrayed in Fig. 3d. The calculated optical constant values have been tabulated in Table 4.

The single effective oscillator model suggested by Wemple–Didomenico [33] has been utilized to deduce the values of dispersive constants which are playing significant role in optical communication and spectral dispersion devices [34].

The model relates the dispersive refractive index  $[n^2(E)]$  with dispersion energy ( $E_1$ ) and average excitation or oscillator energy ( $E_0$ ) as,

$$[n^2(E)] = 1 + [E_1 E_0 / (E_0^2 - E^2)] \quad (25)$$

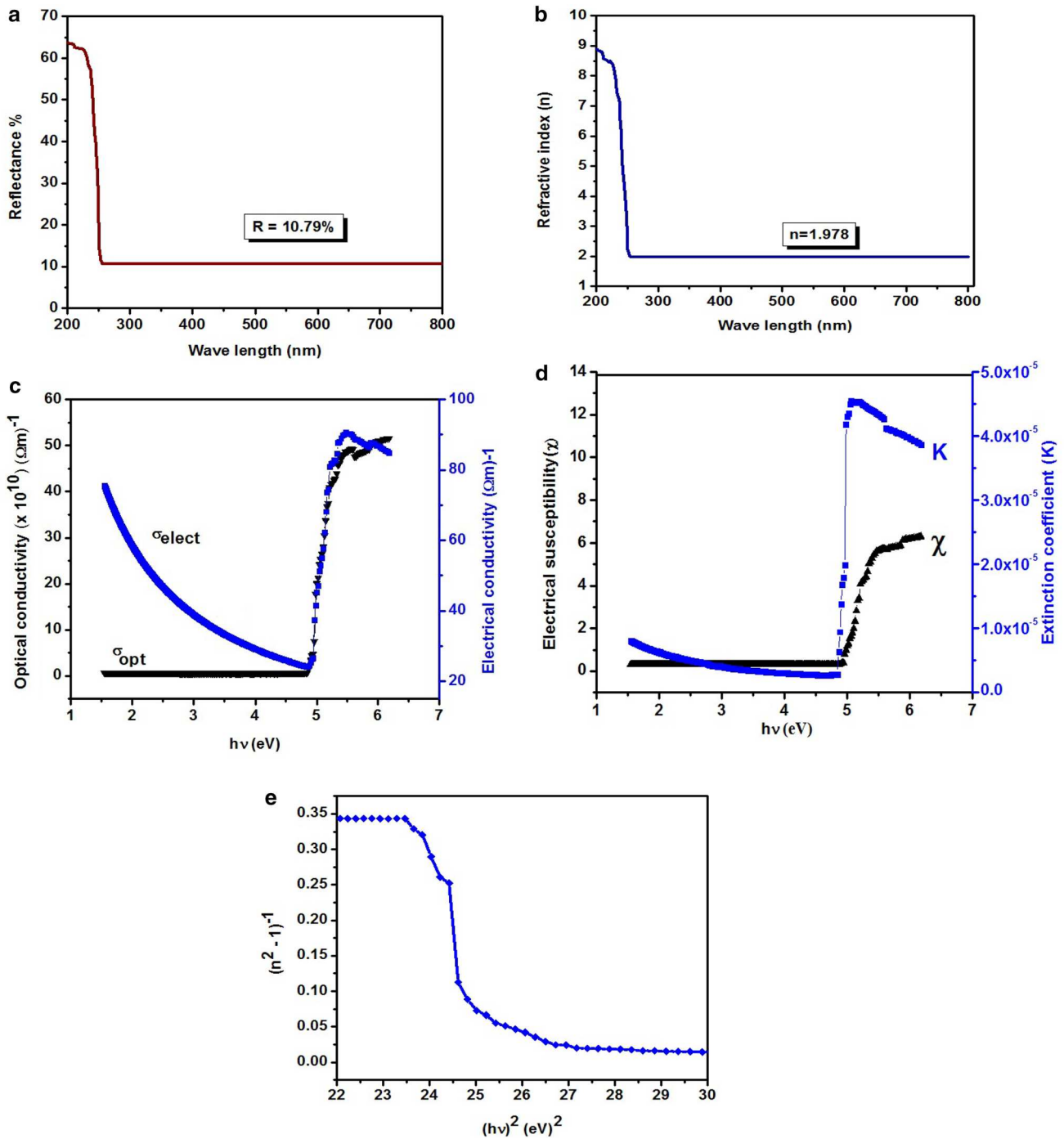


**Fig. 3** **a** Variance of reflectance with wavelength. **b** Variance of refractive index with wavelength. **c** Dependence of conductivities on photon energy. **d** Dependence of electrical susceptibility and extinction coefficient on photon energy. **e** Plot of  $(n^2 - 1)^{-1}$  vs.  $(h\nu)^2$

where  $E = h\nu$ . The slope  $(-1/E_1E_0)$  and intercept  $(E_0/E_1)$  values of the graph (Fig. 3e) plotted between  $(n^2 - 1)^{-1}$  vs.  $(h\nu)^2$  have been utilized to deduce the values of  $E_1$  and  $E_0$ . From the values of  $E_1$  and  $E_0$ , other oscillator parameters such as the oscillator strength ( $f$ ), inter band transition strengths ( $M_{-1}$  and  $M_{-3}$ ), static dielectric constant ( $\epsilon_s$ )

and static refractive index ( $n_s$ ) can be computed using the expressions [35–38],

$$f = E_1E_0 \tag{26}$$

$$M_{-1} = E_1/E_0 \tag{27}$$



**Table 4** Optical constant values of BTAB

Parameter	Symbol	Values
Reflectance (%)	R	10.79
Refractive index	n	1.98
Urbach's energy (eV)	$E_u$	0.16
Real part of dielectric constant	$\epsilon_r$	3.92
Imaginary part of dielectric constant ( $10^{-5}$ )	$\epsilon_i$	3.19
Electrical susceptibility	$\chi$	0.31
Optical conductivity ( $10^9 \Omega\text{m}^{-1}$ )	$\sigma_{\text{op}}$	5.99
Electrical conductivity ( $\Omega\text{m}^{-1}$ )	$\sigma_e$	75.59
Extinction coefficient ( $10^{-6}$ )	K	8.07

$$M_{-3} = E_1 / (E_0)^3 \quad (28)$$

$$\epsilon_s = 1 + M_{-1} \quad (29)$$

$$n_s = (\epsilon_s)^{1/2} \quad (30)$$

The values of single oscillator parameters have been tabulated in Table 5.

The desirous and optimal values of the optical constants and oscillator parameters given in Tables 4 and 5 testify the crystal's applicability in NLO and semi conducting device applications which include anti reflectors, optical computing applications, spectral dispersive instruments and fast information processing devices [39].

### 3.5 Etching Analysis

The process of etching can be described as the selective dissolution of the crystal by an etchant. The capability of revealing etch pits by a solvent on a particular face of a crystal depends on the crystallographic orientation and the symmetry of the crystal face [40]. It is a reverse

phenomenon of crystal growth. Etching studies serve as an excellent tool for assessing structural perfection and accompanied growth features of a grown crystal. The patterns obtained from the etching analysis are of unique nature and are providing useful information on the growth pattern and growth mechanism of the crystal [41]. Etching analysis on BTAB crystal has been carried out using water etchant at room temperature. The etching duration was for 10 s. The etched surfaces were dried by gently pressing them between two wrinkle free tissue paper. The microstructure of the dried crystal has been observed under a reflection mode optical microscope. The recorded etch pattern with rectangular hillocks due to layer growth as shown in Fig. 4, suggested the two-dimensional nucleation mechanism with less dislocations [42].

### 3.6 Phase-Matching and NLO Properties

In the case of bulk crystals to be considered for any SHG device applications, their phase matchable capability will be an added advantage. The phase matching nature of a NLO material is defined as the increase in SHG intensity with the rise in particle size up to a threshold size (average coherence length) and attainment of constant value thereafter. But in the case of non phase-matchable materials, after the coherence length, SHG varies inversely with the particle size [43]. Hence, only the bulk crystals with phase matchable nature will have the inherent tendency to allow the SHG to increase monotonically as the beam passes through them. The phase matching nature and SHG efficiency of the title compound has been analyzed by and Kurtz–Perry SHG test [44]. A Q switched Nd:YAG laser beam ( $\lambda = 1064 \text{ nm}$ ) with an input power of 3 mJ/pulse, along with 8 ns pulse width a repetition rate of 10 Hz has been employed in the analysis. The standard sample taken

**Fig. 4** Etch pattern of BTAB crystal**Table 5** Single oscillator parameter values of BTAB

Parameter	Symbol	Values
Dispersion energy (eV)	$E_1$	17.45
Average excitation energy (eV)	$E_0$	6.91
Oscillator strength ( $\text{eV}^2$ )	f	120.48
Inter band transition strength	$M_{-1}$	2.52
Inter band transition strength ( $\text{eV}^{-2}$ )	$M_{-3}$	0.053
Static dielectric constant	$\epsilon_s$	3.53
Static refractive index	$n_s$	1.88

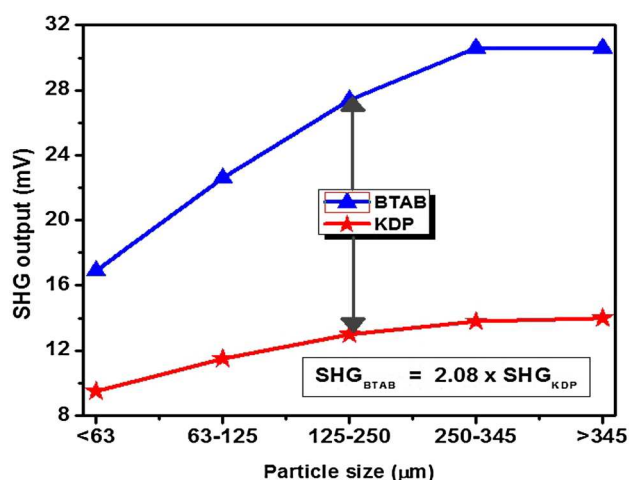


**Fig. 5** Comparison of phase matching SHG efficiency of BTAB and KDP

was Potassium dihydrogen phosphate (KDP). The BTAB and KDP samples were powdered into various grain sizes (<63, 63–125, 125–250, 250–345 and >345 μm) using standard sieves and filled densely and tightly in separate micro-capillary tubes. The polarized laser beam was directed on the samples. The SHG output of wavelength 532 nm, as green light emission, has been detected by the photomultiplier tube which ascertained the frequency doubling efficiency of the samples. From Fig. 5, showing the SHG output values for BTAB and KDP, the phase matching nature of BTAB has been established as its SHG efficiency is increasing up to a size of 250 and after that attaining a constant value. Considering the average values of SHG, it is also interesting to note that the SHG efficiency of the BTAB crystal is 2.08 times that of standard KDP crystal.

### 3.7 Birefringence Studies

Birefringence is defined as the difference between the two refractive indices of ordinary and extraordinary rays. The birefringent crystals deserve a special mention in the field of linear and non-linear optics owing to their viable applicability in the devices like polarization manipulations, light modulator, optical sensors and liquid crystal display units [45]. The qualitative assessment of the crystals through birefringence measurement has been established in literature [46]. The BTAB plates for birefringence analysis have been prepared by cutting and polishing the surface of the crystals and have been used for the Modified Channel Spectrum (MCS) experiment [47]. The crystal plate has been placed between the polarizer and analyser. Then the beam from He–Ne laser source has been made to pass through the crystal plate. Depending on the crystalline nature of

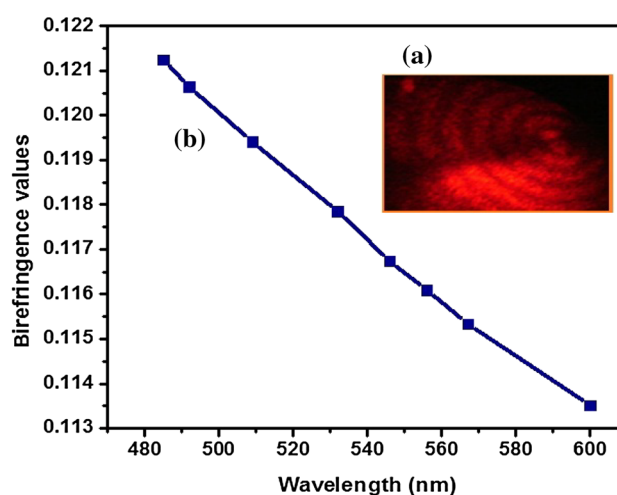


**Fig. 6** a Observed fringe pattern for BTAB crystal. b Plot of birefringence values vs. wavelength

the plate, the transmitted light from the analyser undergoes interference and creates a characteristic fringe pattern on the screen. The obtained birefringence interferogram pattern has been given in Fig. 6a. The regular and uniform fringe pattern authenticated the defects free nature of the crystal with high optical quality. The pattern also signified the homogeneity of refractive index of the material. From the known values of the plate thickness in mm ( $t$ ), corresponding wavelength ( $\lambda$ ) and fringe order ( $k$ ), the birefringence values ( $\Delta n$ ) have been calculated by the expression,

$$\Delta n = k\lambda/t \quad (31)$$

The obtained values of birefringence have been plotted against the wavelength. The trend of the graph, as given in Fig. 6b, showing inverse relationship between birefringence and wavelength is called as negative dispersion of birefringence. The negative dispersive materials find their applications in the laser medium to balance the positive dispersion [48]. The plot shows almost a straight line and indicates that the crystal has highly oriented nature with lesser disorder. The high crystalline nature of the sample and its suitability to be used in harmonic generation devices has been further evidenced by the low birefringence value [49] of 0.118 at the wavelength of 532 nm. Further, in the wavelength range of 480–600 nm, the crystal exhibited the birefringence value from 0.114 to 0.121 which is a nominal variation which supported the suitability of BTAB in SHG and polarization devices.

### 3.8 Photoconductivity Studies

The electrical conductivity exhibited by a material on exposure to various electromagnetic radiations is known as photoconductivity. If the conductivity is enhanced by these

radiations, it is known as positive photoconductivity and if it is suppressed, it is known as negative photoconductivity. By following the photoconductivity experimental set up available in literature [50], studies on the BTAB single crystals have been carried out by connecting the sample in series with a dc power supply and a Keithley 480 pico ammeter at the room temperature. After shielding the sample from all radiations, the dark current ( $I_d$ ) of the crystals has been recorded by applying field voltage of 0–1000 V. Then the sample has been illuminated with halogen lamp source of 100 W with the same field voltage and the photo current ( $I_p$ ) in pico ammeter has been recorded. The field dependent nature of dark and photo currents of BTAB has been shown in Fig. 7. The negative photo conductivity of the BTAB crystal has been witnessed from the graph in which the dark current is more than the photo current for the same applied field. As per Stockmann model, this trend of negative conducting nature of the crystal may be attributed to the reduction in the number or life time of charge carriers in presence of radiation [51]. Since the role of negative photo conducting materials has been favorably established in the field of IR and UV detectors, semiconductor laser technology and optoelectronics [52], BTAB crystals stand a good chance of being utilized in the fore-said domains also.

### 3.9 Dielectric Studies

The dielectric characteristics of the crystals are very important to analyze the lattice dynamics present in them [53]. The study further gives insight into the charge transport mechanism of a material. Non-linear polarization of the crystals with respect to the applied electric field causes the phenomena of non-linear optics to arise. The polarization of the crystals with respect to the applied electric field

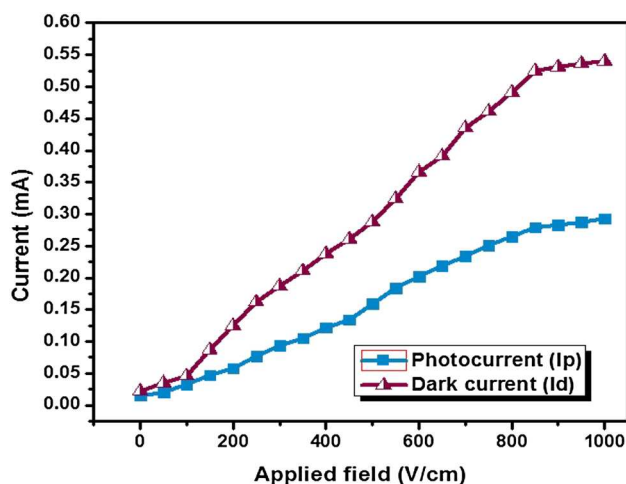


Fig. 7 Field dependent nature of dark and photo current of BTAB

forms the base for dielectric measurements. In view of this, for BTAB crystals, the dielectric measurements have been carried out at the frequency regions of 50 Hz–5 MHz at various temperatures. The dependence of dielectric constant values on applied frequency at various temperatures has been plotted in Fig. 8a which shows at lower frequencies the dielectric constant values are higher. On the other hand, the dielectric constant values continuously decrease with increment in frequency. This trend can be explained by the fact that at low to moderate frequencies, it would be easy for the dipoles to respond and align themselves with the applied alternating electric dipoles whereas at higher frequencies the dipoles cannot cope up with changing electric field. In addition to this effect, space charge polarization resulted from the accumulation of charge at the electrode—sample interface also considered to be the reason for the trend in low frequency zone [54]. In a similar way, at higher frequency zones, suppression of charge carrier contribution due to the high occurrence of periodical reversal at the electrode—sample interface would have resulted in lower values of dielectric constant values [55]. The plot of dielectric loss vs. frequency has been shown in Fig. 8b. The presence of space charge effect may be suitably reasoned for the higher loss value at lower frequencies and quenching of the space charge effect at higher frequencies resulted in the lowering of dielectric loss values [56]. Good quality and defects free nature of the crystal has been evidenced by the low dielectric loss at high frequency [57].

The alternating current conductivity  $\sigma_{ac}$  is calculated by the relationship,

$$\sigma_{ac} = 2\pi f \epsilon_0 \epsilon_r \tan \delta \quad (32)$$

where  $f$  is the frequency of applied field,  $\epsilon_0$  is the absolute permittivity in free space,  $\epsilon_r$  is the real part of dielectric permittivity and  $\tan \delta$  is loss tangent. The activation energy ( $E_a$ ) of the electrical process can be obtained from an Arrhenius plot using the equation,

$$\sigma_{ac} = \sigma_0 \exp(-E_a/kT) \quad (33)$$

where  $k$  is Boltzmann constant and  $\sigma_0$  implies the conductivity at temperature  $T$ . From the slope obtained from a plot between  $\ln \sigma_{ac}$  vs.  $1000/T$ , as shown in Fig. 8c, the activation energy ( $E_a$ ) values may be deduced as,

$$E_a = (-\text{Slope}) \times 1000 \times \text{Boltzmann constant} \quad (34)$$

For the applied frequencies of 1, 5, 10, 50 and 100 KHz, the activation energy has been calculated as 0.119, 0.067, 0.048, 0.035 and 0.025 eV respectively. Such low value of activation energy is one of the salient features of the crystals with minimum defects and high crystallinity [58]. The SHG efficiency of a material may be further evidenced by certain special properties such as valence electron plasma energy ( $\hbar\omega_p$ ), Penn gap ( $E_p$ ), Fermi energy ( $E_f$ ) and polarisability

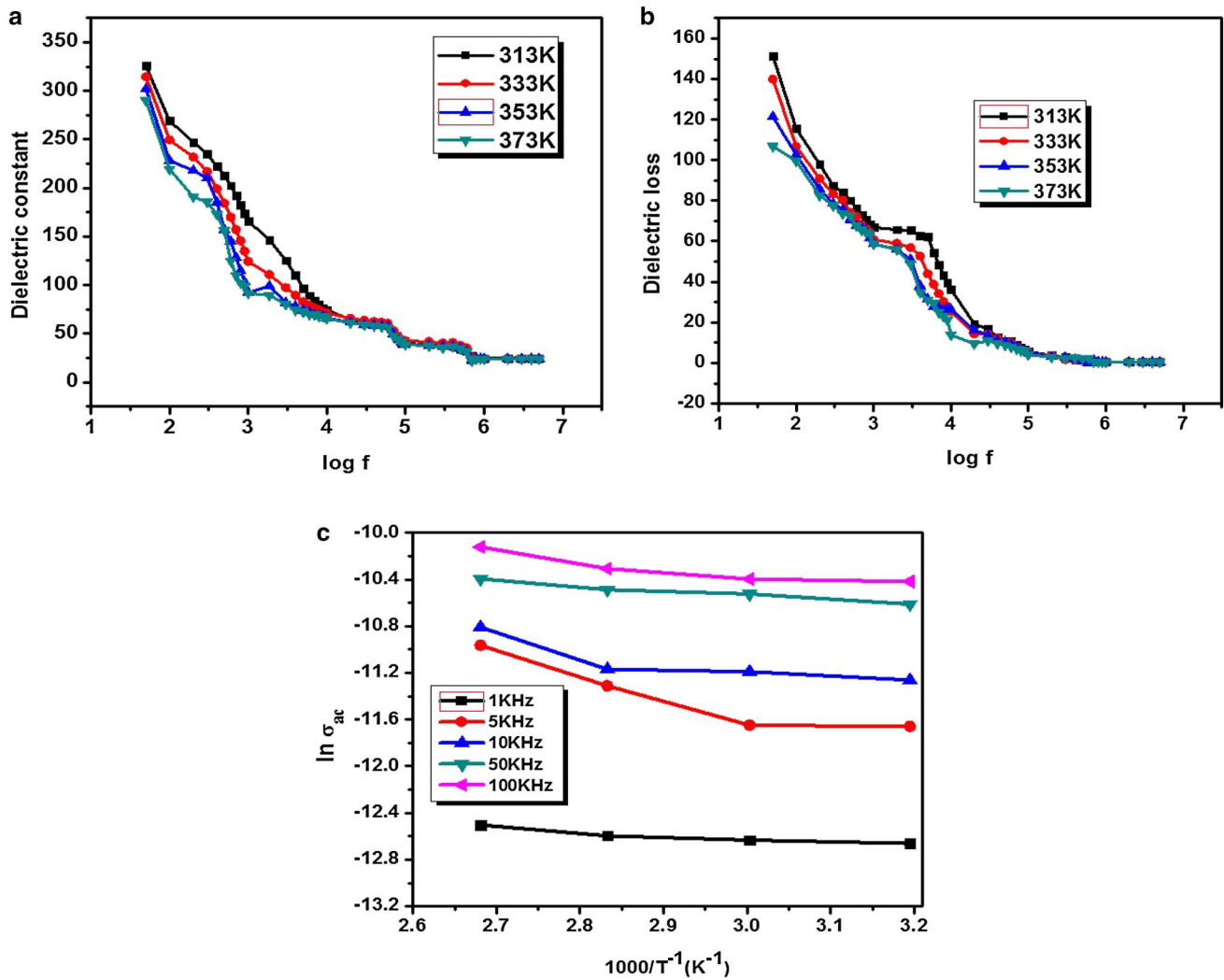


**Fig. 8** **a** Plot of dielectric constant dependency on applied frequency. **b** Plot of dielectric loss dependency on applied frequency. **c** Plot of  $\ln \sigma_{ac}$  vs.  $1000/T^{-1}$

( $\alpha_p$ ) which are collectively grouped as solid state parameters. With respect to BTAB crystals, from the values of its density ( $\rho=2.6480 \text{ g cm}^{-3}$ ), number of valence electrons ( $Z=74$ ), molecular weight ( $M=513.72$ ) and saturated dielectric constant value ( $\epsilon_{\infty}=24.1$ ), it is possible to arrive at the values of these solid state parameters by the following expressions [59],

$$\alpha_p = [(\hbar\omega_p)^2 S_0 / \{(\hbar\omega_p)^2 S_0 + 3E_p^2\}] \times (M/\rho) \times 0.396 \times 10^{-24} \tag{35}$$

where  $S_0$  is a material specific constant. Further,

$$\hbar\omega_p = 28.8[(Z.\rho)/M]^{1/2} \tag{36}$$

where  $\hbar = h/2\pi$ ,  $\omega_p$  is the plasma angular frequency.

$$E_p = \hbar\omega_p / (\epsilon_{\infty-1})^{1/2} \tag{37}$$

$$S_0 = 1 - \{ (E_p / 4E_F) \} + \{ 1/3 \} (E_p / 4E_F)^{1/2} \tag{38}$$

$$E_F = 0.2948 (\hbar\omega_p)^{4/3} \tag{39}$$

Yet another form of polarisability calculation has been in the form of Claussius–Mossotti equation [60] as,

$$\alpha_p = (3M/4\pi N\rho) \times (\epsilon_{\infty-1} / \epsilon_{\infty+2}) \tag{40}$$

where  $N$  is Avogadro number.

The value of  $\alpha_p$  can also be deduced from the value of band gap ( $E_g$ ) [61] as per the expression,

$$\alpha_p = \left[ 1 - \left( \sqrt{E_g} / 4.06 \right) \right] \times (M/\rho) \times 0.396 \times 10^{-24} \tag{41}$$

**Table 6** Solid state parameters of BTAB

Parameters	Symbol	Values
Plasma energy (eV)	$\hbar\omega_p$	17.79
Penn gap (eV)	$E_p$	3.70
Fermi energy (eV)	$E_F$	13.69
Material constant	$S_0$	0.94
Polarisability by Penn gap ( $\times 10^{-23}$ cm <sup>3</sup> )	$\alpha_p$	6.75
Polarisability by Clausius–Mosotti equation ( $\times 10^{-23}$ cm <sup>3</sup> )	$\alpha_p$	6.81
Polarisability by band gap energy ( $\times 10^{-23}$ cm <sup>3</sup> )	$\alpha_p$	3.47

The obtained solid state parameter values have been tabulated in Table 6 and the higher values of polarisability and related parameters signify the NLO nature of BTAB crystals.

### 3.10 Mechanical Studies

The hardness of a material is defined as the resistance it offers to the motion of dislocations, deformations or damage under an applied stress [62]. The micro indentation hardness studies provide valuable information on the glide, deformation, cracks, grain boundary hardening, anisotropy, dispersion of impurity, environment of dislocation mobility and quench hardening effect of irradiation [63]. In the process of Vicker's hardness testing, crack free and smooth crystal of BTAB was mounted on the microscope base and indentations have been made gently on the crystal at room temperature with the loads varying from 25 to 100 g in steps of 25 g for an indentation time of 10 s. For each load five well defined indentations were measured and the average diagonal length ( $d$  in mm) has been employed to calculate the hardness number ( $H_v$ ) from the equation,

$$H_v = 1.8544P/d^2, \quad (42)$$

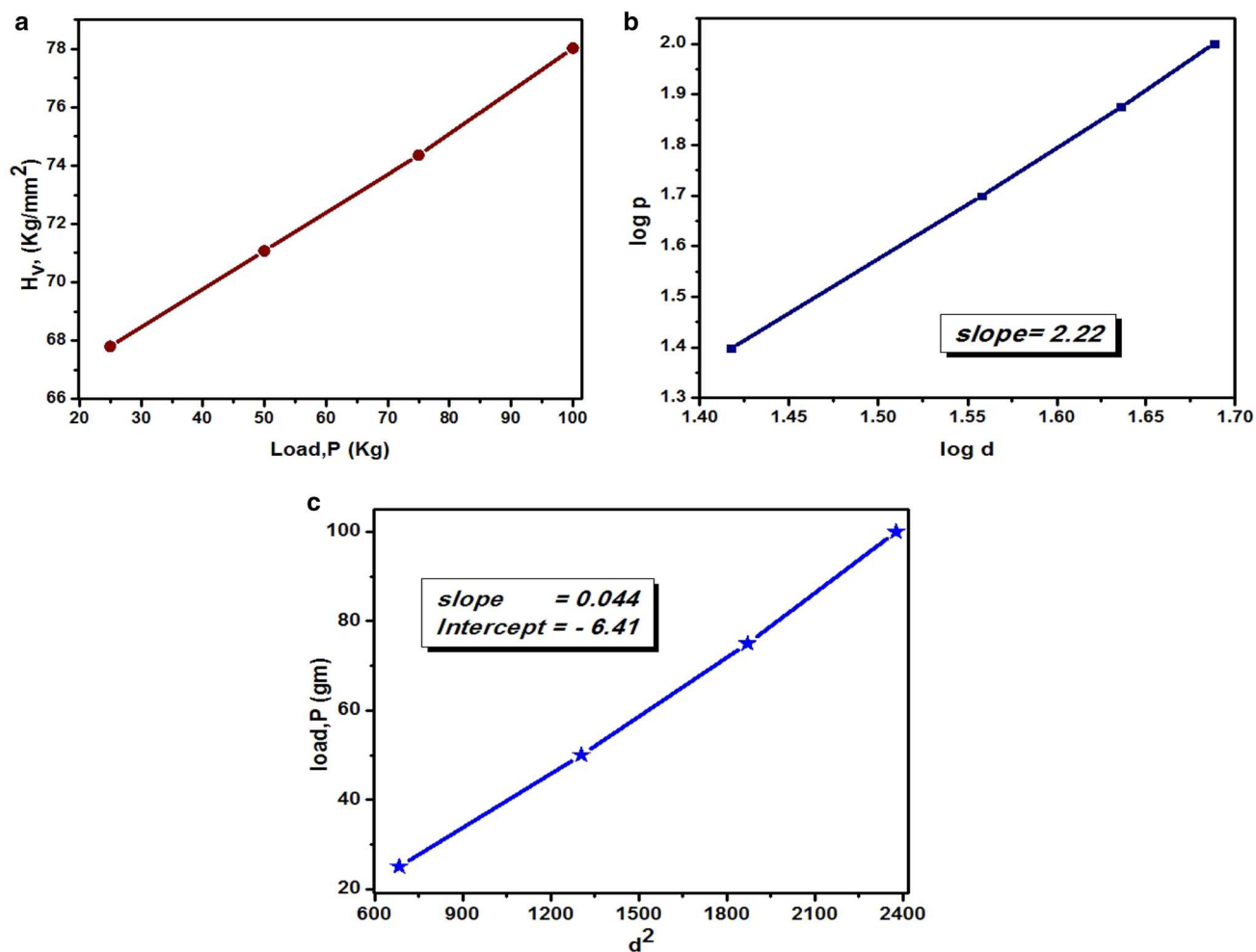


**Fig. 9** **a** Plot of hardness number vs. applied load. **b** Plot of log  $P$  vs. log  $d$ . **c** Plot of  $P$  vs.  $d^2$

**Table 7** Mechanical parameters of BTAB

Load, P (gm)	Hardness number, $H_v$ (Kg/mm <sup>2</sup> )	Elastic stiffness constant, $C_{11}$ (GPa)	Yield strength $\sigma_v$ (Gpa)	Moh's hardness number	c/a value	Type of crack	Fracture toughness ( $K_C$ ) (g/ $\mu\text{m}^{1/2}$ )	Brittleness index ( $B_i$ ) ( $10^3 \mu\text{m}^{-1/2}$ )	Elastic Modulus (E)
25	67.80	15.70	2.36	2.75	1.53	Palmqvist	17.75	3.82	193.34
50	71.07	17.05	2.47	2.79	1.77	Palmqvist	34.55	2.06	202.67
75	74.35	18.46	2.59	2.83	1.85	Palmqvist	54.05	1.38	212.03
100	78.03	20.08	2.72	2.88	2.01	Palmqvist	70.17	1.11	222.52

where P is the applied load in Kg. A plot of  $H_v$  vs. P (Fig. 9a) indicates the reverse indentation size effect in which the hardness number increases with increasing load [64]. Actually, in the initial stages of low loads, plastic deformation of crystals involves nucleation of dislocations along a particular slip system. At higher loads, dislocation multiplications, cross-slip phenomenon and Frank–Read sources are becoming predominant and resulting in an increase in hardness value with applied load [65].

As per Meyer's law [66], if the Meyer's index value is greater than 2, such material will show RISE pattern [64]. The Meyer law states that

$$P = k_1 d^n \quad (43)$$

where  $k_1$  is the material constant and  $n$  is Meyer's index. The slope of a graph drawn between  $\log P$  and  $\log d$  (Fig. 9b) gives the value of  $n$ . As per Hays–Kendall's theory [67],

$$P - W = k_2 d^2 \quad (44)$$

where  $W$  is the minimum load to initiate plastic deformation (Newtonian resultant pressure) and  $k_2$  is a load independent constant.

The slope and intercept of the graph drawn between  $P$  and  $d^2$  (Fig. 9c) are giving the value of  $W$  and  $k_2$  respectively. This theory also suggests that the negative intercept of such graph will result in RISE pattern. Thus the results of Meyer's relation ( $n=2.22$ ) and Heys–Kendall's relation (intercept =  $-6.41$ ) further support the RISE pattern exhibited by the BTAB crystal. Based on the  $n$  value, Onistch [68] classified the materials into soft and hard materials. According to this rule, the hard materials will have  $n$  value between 1 and 1.6 and the soft materials will have  $n$  value  $>1.6$ . Hence, BTAB has been found to be coming under soft material category.

The value of hardness number is also used to calculate the elastic stiffness constant ( $C_{11}$ ), elastic modulus (E), yield strength ( $\sigma_v$ ) and Mohs hardness number by the expressions [69–71],

$$C_{11} = (H_v)^{7/4} \quad (45)$$

$$E = 81.9635H_v \quad (46)$$

$$\sigma_v = \{H_v/2.9\} \times \{[1 - (n - 2)] \times [12.5(n - 2)/1 - (n - 2)]^{n-2}\} \quad (47)$$

$$H_M = 0.675 \times (H_v)^{1/3} \quad (48)$$

Another important mechanical parameter, fracture toughness ( $K_C$ ) is used to indicate the extend of fracture stress exerted on the material under consistent loading. As per Proton-Rawling classification [72], Median type of cracks will prevail in the crystals having the  $c/a$  ratio (where  $c$  is the crack length in  $\mu\text{m}$  and  $a=d/2$ ) greater than or equal to 2.5 whereas the crack type will be Palmvist if the ratio is  $<2.5$ . The hardness analysis on BTAB suggested the Palmqvist cracks whose  $K_c$  is given by,

$$K_C = kPa/l^{1/2} \quad (49)$$

Such that,  $l=c-a$ ,  $k$  is the constant whose value is equal to  $1/7$  for the Vickers indenter. Yet another mechanical constant, known as Brittleness index ( $B_i$ ) gives an idea about the fracture induced in a material, is calculated from the expression [73],

$$B_i = H_v/K_C \quad (50)$$

The calculated important mechanical parameters have been tabulated in Table 7. As the hardness value is high, more stress is required to form dislocation and hence the higher hardness values indicate crystalline perfection of the sample. Higher value of elastic stiffness constant attests the higher strength of binding forces [74] and higher value of elastic modulus and fracture toughness typify greater rigidity of the crystals [70].

## 4 Conclusion

The semi organic non-linear crystals of bis(thiourea) antimony tribromide single crystals have been successfully grown by the slow solvent evaporation technique

using water solvent. The values of calculated nucleation parameters such as meta stable zone width, induction period, interfacial surface energy, critical free energy, free energy change, critical radius, critical number and nucleation rate supported the preferred growth of the BTAB crystals. The axial lengths, orthorhombic structure and  $Cmc_2_1$  space group have been inferred by single crystal X-ray diffraction analysis. The elemental analysis has been performed in order to elucidate the constituents and composition percentage of BTAB crystal. The values of various optical and oscillator parameters comprising of transmittance, band gap energy, reflectance, refractive index, extinction coefficient, optical conductivity, susceptibility, Urbach's energy, dispersion energy, average excitation energy, static refractive index and oscillator strength have been computed through the UV spectral studies in order to verify the required NLO quality of the crystal. The layer growth two dimensional nucleation mechanism has been revealed by etching analysis. Confirming the phase matching nature of the BTAB crystals, the Kurtz–Perry technique also indicated that BTAB has 2.02 times SHG efficiency as that of standard KDP. The photo conductivity studies resulted in the negative photo conductive nature of BTAB crystal which enables its utilization in optoelectronic devices. The uniform fringe pattern and low birefringence value of BTAB have signaled the suitability of the crystal in optical devices. The defects free nature of the crystals has been further indicated by its low dielectric constant and dielectric loss at higher electrical frequencies. The lower activation energy of electrical process testified the homogeneity and crystallinity of the crystal. The derived solid state parameters like polarisability, Fermi energy and Penn gap have further provided evidence for the SHG efficiency of the BTAB crystals. The mechanical parameters (hardness number, Meyer's index, elastic stiffness constant, yield strength, fracture toughness, elastic modulus and brittleness index) resulting from Vicker's micro hardness analysis proved the mechanical strength of the BTAB crystal needed for laser applications. Thus, based on the findings discussed above, the suitability and reliability of BTAB crystals in NLO applications have been effectively justified.

**Acknowledgements** The authors express their thanks to B.S. Abdul Rahman University, Chennai; PG and research Department of Chemistry, Dr. Ambedkar Govt. Arts College, Vyasarpadi; SAIF-Indian Institute of Technology, Chennai; St. Joseph's College of Engineering, Chennai; University of Madras, Guindy campus; IISc, Bengaluru; St. Joseph College, Trichy for extending their lab facilities towards the research studies.

## References

1. S.S. Hussaini, N.R. Dhumane, G. Rabbani, P. Karmuse, V.G. Dongre, M.D. Shirsat, Growth and high frequency dielectric study of pure and thiourea doped KDP crystals. *Cryst. Res. Technol.* **42**, 1110–1116 (2007)
2. S. Ariponnammal, S. Radhika, N. Victorjaya, High pressure electrical resistivity study on nonlinear single crystal zinc thiourea sulphate (ZTS). *Cryst. Res. Technol.* **40**, 786–788 (2005). doi:10.1002/crat.200410432
3. S.M. RaviKumar, N. Melikechi, S. Selvakumar, P. Sagaraj, Studies on the optical, thermal and electrical properties of bis(thiourea) cadmium formate NLO crystals. *Phys. B Condens. Matter* **403**, 4160–4163 (2008). doi:10.1016/j.physb.2008.08.022
4. J.G.S. Lopes, L.F.C. de Oliveira, H.G.M. Edwards, P.S. Santos, The Raman spectrum of thiourea–oxocarbon adducts. *J. Raman Spectrosc.* **35**, 131–139 (2004). doi:10.1002/jrs.1113
5. N.R. Rajagopalan, P. Krishnamoorthy, A systematic approach to physico–chemical analysis of tris(thiourea) zinc selenate: a semi-organic nonlinear optical crystal. *Optik* **129**, 118–129 (2017). doi:10.1016/j.ijleo.2016.10.039
6. V. Rajendran, J. Uma, Synthesis, structural, topographical, linear and nonlinear optical, electrical and mechanical properties of bithiourea zinc acetate single crystal. *Opt. Mater.* **57**, 249–256 (2016). doi:10.1016/j.optmat.2016.05.006
7. N.R. Rajagopalan, P. Krishnamoorthy, K. Jayamoorthy, A strategic approach to physico–chemical analysis of bis(thiourea) lead chloride: a reliable semi-organic nonlinear optical crystal. *Opt. Laser Technol.* **89**, 6–15 (2017). doi:10.1016/j.optlastec.2016.10.001
8. R. Uthrakumar, C. Vesta, C. Justin Raj, S. Krishnan, S. Jerome Das, Bulk crystal growth and characterization of non-linear optical bithiourea zinc chloride single crystal by unidirectional growth method. *Curr. Appl. Phys.* **10**, 548–552 (2010). doi:10.1016/j.cap.2009.07.018
9. N.R. Rajagopalan, P. Krishnamoorthy, Contemporary studies on growth and characterization of bis(thiourea) strontium chloride: a potential optoelectronic NLO material. *Optik* **127**, 3582–3589 (2016). doi:10.1016/j.ijleo.2015.12.153
10. N. Karthik, R. Sankar, R. Jayavel, S. Pandi, Synthesis, growth and characterization of semi-organic non-linear optical bis thiourea antimony tribromide single crystals. *J. Cryst. Growth* **312**, 114–119 (2009). doi:10.1016/j.jcrysgro.2009.09.054
11. N.P. Rajesh, V. Kannan, P. Santhana Raghavan, P. Ramasamy, C.W. Lan, Nucleation studies and crystal growth of  $(NH_4)_2H_2PO_4$  doped with thiourea in super saturated aqueous solutions. *Mater. Chem. Phys.* **76**, 181–186 (2002). doi:10.1016/S0254-0584(01)00525-9
12. N.P. Zaitseva, L.N. Rashkovich, S.V. Bogatyreva, Stability of  $KH_2PO_4$  and  $K(H, D)_2PO_4$  solutions at fast crystal growth rates. *J. Cryst. Growth* **148**, 276–282 (1995). doi:10.1016/0022-0248(94)00606-7
13. H. El-shall, Jin-Hwan Jeon, E.A. Abdel, S. Khan, L. Gower, Y. Rabinovich, A study of primary nucleation of calcium oxalate monohydrate: I-effect of supersaturation. *Cryst. Res. Technol.* **39**, 214–221 (2004). doi:10.1002/crat.200310173
14. M. Volmer, A. Weber, Keimbildung in übersättigten Gebilden (nucleus formation in super saturated systems). *Z. Phys. Chem. Abt. A* **119**, 277–301 (1926)
15. A. Siva Dhas, P. Selvarajan, T.H. Freeda, Nucleation kinetics, growth and XRD studies of undoped and zinc sulfate-doped triglycine sulpho-phosphate (TGSP) crystals. *Mater. Manuf. Proc.* **24**, 584–589 (2009)

16. P. Bennema, O. Sohnel, Interfacial surface tension for crystallization and precipitation from aqueous solutions. *J. Cryst. Growth* **102**, 547–556 (1990). doi:[10.1016/0022-0248\(90\)90412-E](https://doi.org/10.1016/0022-0248(90)90412-E)
17. J. Christoffersen, E. Rostrup, M.R. Christoffersen, Relation between interfacial surface tension of electrolyte crystal in aqueous suspension and their solubility: a simple derivation based on surface nucleation. *J. Cryst. Growth* **113**, 599–605 (1991). doi:[10.1016/0022-0248\(91\)90096-N](https://doi.org/10.1016/0022-0248(91)90096-N)
18. A.E. Nielson, O. Sohnel, Interfacial tensions electrolyte crystal-aqueous solution, from nucleation data. *J. Cryst. Growth* **11**, 233–242 (1971). doi:[10.1016/0022-0248\(71\)90090-X](https://doi.org/10.1016/0022-0248(71)90090-X)
19. F. Feigl, V. Anger, *Spot Tests in Inorganic Analysis*, 6th edn. (Elsevier, New York, 2012), p. 529
20. M. Toulemonde, C. Dufour, E. Paumier, Transient thermal process after a high-energy heavy-ion irradiation of amorphous metals and semiconductors. *Phys. Rev. B* **46**, 14362–14369 (1992). doi:[10.1103/PhysRevB.46.14362](https://doi.org/10.1103/PhysRevB.46.14362)
21. N.R. Dhumane, S.S. Hussaini, V.G. Dongre, M.D. Shirsat, Influence of glycine on the nonlinear optical properties of zinc (tris) thiourea sulfate (ZTS) single crystal. *Opt. Mater.* **31**, 328–332 (2008). doi:[10.1016/j.optmat.2008.05.002](https://doi.org/10.1016/j.optmat.2008.05.002)
22. P.M. Ushashree, R. Jayavel, C. Subramanian, P. Ramasamy, Growth of zinc thiourea sulfate (ZTS) single crystals: a potential semiorganic NLO material. *J. Cryst. Growth* **197**, 216–220 (1999). doi:[10.1016/S0022-0248\(98\)00906-3](https://doi.org/10.1016/S0022-0248(98)00906-3)
23. J. Tauc, R. Grigorovici, A. Vancu, Optical properties and electronic structure of amorphous germanium. *Phys. Status Solid. B* **15**, 627–637 (1966). doi:[10.1002/pssb.19660150224](https://doi.org/10.1002/pssb.19660150224)
24. F. El-Diasty, F.A. Abdel Wahab, M. Abdel-baki, Optical band gap studies on lithium aluminium silicate glasses doped with Cr<sup>3+</sup> ions. *J. Appl. Phys.* **100**, 093511-1-7 (2006). doi:[10.1063/1.2362926](https://doi.org/10.1063/1.2362926)
25. A.M. AbdulWahab, Influence of temperature on the optical properties of zinc tris-thiourea sulfate (ZTS) single crystal. *Opt. Mater.* **35**, 146–154 (2012). doi:[10.1016/j.optmat.2012.07.015](https://doi.org/10.1016/j.optmat.2012.07.015)
26. S. Banerjee, A. Kumar, Swift heavy ion induced modifications in the optical band gap and Urbach's tail in polyaniline nanofibres. *Nucl. Instrum. Methods Phys. Res. Sect. B* **269**, 2798–2806 (2011). doi:[10.1016/j.nimb.2011.09.004](https://doi.org/10.1016/j.nimb.2011.09.004)
27. S.M.N. Priya, B. Varghese, J.M. Linet, G. Bhagavannarayana, C.J. Raj, S. Krishnan, S. Dinakaran, S. Jerome Das, Growth, and characterization of novel non-linear optical active dichloridodiglycine zinc dihydrate single crystals. *Cryst. Growth Des.* **8**(5) 1663–1667 (2008). doi:[10.1021/cg701162j](https://doi.org/10.1021/cg701162j)
28. M. Rigana Begam, N. Madhushadhana rao, S. Kaleemulla, N. Sai Krishna, M. Kuppan, G. Krishnaiah, J. Subrahmanyam, Room temperature ferro magnetism in Cd<sub>1-x</sub>Cr<sub>x</sub>Te diluted magnetic semiconductor crystal. *Mater. Sci. Semicond. Proc.* **18**, 146–151 (2014). doi:[10.1016/j.mssp.2013.11.017](https://doi.org/10.1016/j.mssp.2013.11.017)
29. D.D.O. Eya, A.J. Ekpunobi, C.E. Okeke, Influence of thermal annealing on the optical properties of tin oxide thin films prepared by chemical bath deposition technique. *Acad. Open Internet J.* **17**, 1–10 (2006)
30. M.S. Shakeri, M. Rezvani, Optical band gap and spectroscopic study of lithium alumino silicate glass containing Y<sup>3+</sup> ions. *Spectrochim. Acta, Part A* **79**, 1920–1925 (2011). doi:[10.1016/j.saa.2011.05.090](https://doi.org/10.1016/j.saa.2011.05.090)
31. N.F. Mott, E.A. Davis, *Electronic Process in Non-Crystalline Materials*, 2nd edn. (Clarendon, Oxford, 1979)
32. P.V. Dhanaraj, T. Suthan, N.P. Rajesh, Synthesis, crystal growth and characterization of a semiorganic material: calcium dibromide bis(glycine) tetrahydrate. *Curr. Appl. Phys.* **10**(2010) 1349–1353 (2010). doi:[10.1016/j.cap.2010.04.008](https://doi.org/10.1016/j.cap.2010.04.008)
33. S.H. Wemple, M. DiDomenico, Behavior of the electronic dielectric constant incovalent and ionic materials. *Phys. Rev. B* **3**, 1338–1351 (1971). doi:[10.1103/PhysRevB.3.1338](https://doi.org/10.1103/PhysRevB.3.1338)
34. M.M. El-Nahass, A.H. Ammar, A.A. Atta, A.A.M. Farag, E.F.M. El-Zaidia, Influence of X-ray irradiation on the optical properties of CoMTPP thin films. *Opt. Commun.* **284**, 2259–2263 (2011). doi:[10.1016/j.optcom.2010.12.032](https://doi.org/10.1016/j.optcom.2010.12.032)
35. S.H. Wemple, M. DiDomenico, Optical dispersion and structure of solids. *J. Phys. Rev. Lett.* **23**(20) 1156–1160 (1969). doi:[10.1103/PhysRevLett.23.1156](https://doi.org/10.1103/PhysRevLett.23.1156)
36. S.H. Wemple, Refractive-index behavior of amorphous semiconductors and glasses. *Phys. Rev. B Condens. Matter* **7**, 3767–3777 (1973). doi:[10.1103/PhysRevB.7.3767](https://doi.org/10.1103/PhysRevB.7.3767)
37. A.F. Qasrawi, Temperature dependence of the band gap, refractive index and single-oscillator parameters of amorphous indium selenide thin films. *Opt. Mater.* **29**, 1751–1755 (2007). doi:[10.1016/j.optmat.2006.09.009](https://doi.org/10.1016/j.optmat.2006.09.009)
38. A.F. Qasrawi, N.M. Gasanly, Optical properties of Tl<sub>2</sub>InGaS<sub>4</sub> layered single crystal. *Opt. Mater.* **29**, 1763–1767 (2007). doi:[10.1016/j.optmat.2006.09.008](https://doi.org/10.1016/j.optmat.2006.09.008)
39. T.C. Sabari Girisun, S. Dhanuskodi, Linear and non-linear optical properties of tris thiourea zinc sulphate single crystals. *Cryst. Res. Technol.* **44**, 1297–1302 (2009). doi:[10.1002/crat.200900351](https://doi.org/10.1002/crat.200900351)
40. P.M. Ushashree, R. Jayavel, Growth and micromorphology of as-grown and etched bis(thiourea) cadmium chloride (BTCC) single crystals. *Opt. Mater.* **21**, 599–604 (2002). doi:[10.1016/S0925-3467\(02\)00208-2](https://doi.org/10.1016/S0925-3467(02)00208-2)
41. S. Sagadevan, Studies on optical, mechanical, dielectric properties of bithiourea nickel bromide NLO single crystal. *Optik* **125**, 6746–6750 (2014). doi:[10.1016/j.ijleo.2014.08.059](https://doi.org/10.1016/j.ijleo.2014.08.059)
42. S. Mukerji, T. Kar, Etch pit study of different crystallographic faces of L-arginine hydrobromide monohydrate (LAHBR) in alcohols. *J. Cryst. Growth* **200**, 543–549 (1999). doi:[10.1016/S0022-0248\(98\)01251-2](https://doi.org/10.1016/S0022-0248(98)01251-2)
43. A. Sonoc, M. Samoc, P.N. Prasad, A. Krajewska-Cizio, Second-harmonic generation in the crystalline complex antimony triiodide-sulfur. *J. Opt. Soc. Am. B* **9**, 1819–1824 (1992). doi:[10.1364/JOSAB.9.001819](https://doi.org/10.1364/JOSAB.9.001819)
44. S.K. Kurtz, T.T. Perry, A powder technique for the evaluation of non-linear optical materials. *J. Appl. Phys.* **39**, 3798–3812 (1968). doi:[10.1063/1.1656857](https://doi.org/10.1063/1.1656857)
45. K. Buse, M. Luennemann, 3D imaging: wave front sensing utilizing a birefringent crystal. *Phys. Rev. Lett.* **85**, 3385–3387 (2000). doi:[10.1103/PhysRevLett.85.3385](https://doi.org/10.1103/PhysRevLett.85.3385)
46. S. Kar, S. Verma, K.S. Bartwal, Growth optimization and optical characteristics of Fe doped LiNbO<sub>3</sub> crystals. *Cryst. Growth Des.* **8**, 4424–4427 (2008). doi:[10.1021/cg800163f](https://doi.org/10.1021/cg800163f)
47. N. Vijayan, K. Nagarajan, AMZ slawin, C.K. Shasidharan Nair, G. Bhagavannarayana, Growth of benzimidazole single crystal by Sankaranarayanan–Ramasamy method and its characterization by high-resolution x-ray diffraction, thermogravimetric/differential thermal analysis, and birefringence studies. *Crys. Growth Des.* **7**(2), 445–448 (2007). doi:[10.1021/cg0605180](https://doi.org/10.1021/cg0605180)
48. R.L. Fork, O.E. Martinez, J.P. Gordon, Negative dispersion using pairs of prisms. *Opt. Lett.* **9**, 150–152 (1984). doi:[10.1364/OL.9.000150](https://doi.org/10.1364/OL.9.000150)
49. P. Krishnan, K. Gayathri, P.R. Rajkumar, V. Jayaramkrishnan, S. Gunasekaran, G. Anbalagan, Studies on crystal growth, vibrational, optical, thermal and dielectric properties of new organic non-linear optical crystal: bis(2,3-dimethoxy-10-oxostrychnidinium) phthalate nonahydrate single crystal. *Spectrochim. Acta Part A* **131**, 114–124 (2014). doi:[10.1016/j.saa.2014.03.040](https://doi.org/10.1016/j.saa.2014.03.040)
50. F.P. Xavier, A. Regis Inigo, G.J. Goldsmith, Role of metal phthalocyanine in redox complex conductivity of polyaniline and aniline black. *J. Porphyrins Phthalocyanines* **3**, 679–690 (1999). doi:[10.1002/\(SICI\)1099-1409\(199908/10\)3:6/7<679::AID-JPPI96>3.0.CO;2-C](https://doi.org/10.1002/(SICI)1099-1409(199908/10)3:6/7<679::AID-JPPI96>3.0.CO;2-C)



51. S. Abraham Rajasekar, K. Thamizharasan, J.G.M. Jesudurai, D. Prem Anand, P. Sagayaraj, The role of metallic dopants on the optical and photoconductivity properties of pure and doped potassium pentaborate ( $\text{KB}_5$ ) single crystals. *Mater. Chem. Phys.* **84**, 157–161 (2004). doi:10.1016/j.matchemphys.2003.11.017
52. B. Babu, J. Chandrasekaran, S. Balaprabhakaran, P. Ilayabarithi, Optical, structural and electrical properties of pure and urea doped KDP crystals. *Mater. Sci. Poland* **31**, 151–157 (2013). doi:10.2478/s13536-012-0082-4
53. R. Uthrakumar, C. Vesta, G. Bhagavannarayana, R. Robert, S. Jerome Das, Optical, crystalline perfection and mechanical studies on unidirectional grown bis(thiourea) cadmium zinc chloride single crystal. *J. Alloy Comp.* **509**, 2343–2347 (2011). doi:10.1016/j.jallcom.2010.11.015
54. N. Ponpandian, P. Balaya, A. Narayanasamy, Electrical conductivity and dielectric behaviour of nanocrystalline  $\text{NiFe}_2\text{O}_4$  spinel. *J. Phys. Condens. Matter.* **14**, 3221–3237 (2002). doi:10.1088/0953-8984/14/12/311
55. S. Ramesh, M.F. Chai, Conductivity, dielectric behavior and FTIR studies of high molecular weight poly(vinylchloride)–lithium triflate polymer electrolytes. *Mat. Sci. Eng B* **139**, 240–245 (2007). doi:10.1016/j.mseb.2007.03.003
56. S. Hirano, P.C. Kim, H. Orihara, H. Umeda, Y. Ishibasi, Dielectric properties of hydro-thermally grown gallium orthophosphate single crystals. *J. Mater. Sci.* **25**, 2800–2804 (1990). doi:10.1007/BF00584883
57. M. Meena, C.K. Mahadevan, Growth and electrical characterization of L-arginine added KDP and ADP single crystals. *Cryst. Res. Technol.* **43**, 166–172 (2008). doi:10.1002/crat.200711064
58. N. Goel, N. Sinha, B. Kumar, Growth and properties of sodium tetra borate deca hydrate single crystals. *Mater. Res. Bull.* **48**, 1632–18636 (2013). doi:10.1016/j.materresbull.2013.01.007
59. N.M. Ravindra, R.P. Bharadwaj, K. Sunil Kumar, V.K. Srinivas-tava, Model based studies of some optical and electronic properties of narrow and wide gap materials. *Infrared Phys.* **21**, 369–381 (1981). doi:10.1016/0020-0891(81)90045-2
60. D. Anbuselvi, J. Elberin Mary Therasa, D. Jayaraman, V. Joseph, Nucleation kinetics, growth and analysis of structural, optical, dielectric and mechanical properties of non-linear optical material: l-proline manganese chloride. *Phys. B* **423**, 38–44 (2013). doi:10.1016/j.physb.2013.04.049
61. R.R. Reddy, Y. Nazeer Ahammed, M. Ravi Kumar, Variation of magnetic susceptibility with electronic polarizability in compound semiconductors and alkali halides. *J. Phys. Chem. Solids* **56**, 825–829 (1995). doi:10.1016/0022-3697(94)00268-1
62. S. Mukerji, T. Kar, Vicker's microhardness studies of L-arginine hydrobromide mono hydrate crystals (LAHBr). *Cryst. Res. Technol.* **34**, 1323–1328 (1999). doi:10.1002/(SICI)1521-4079(199912)34:10<1323::AID-CRAT1323>3.0.CO;2-4
63. J. Kumar, M. Thirumavalavan, F.D. Gnanam, P. Ramasamy, Microindentation studies on single crystals of sodium and ammonium fluoroborates. *Phys Status Solid (a)* **103**, 431–434 (1987). doi:10.1002/pssa.2211030212
64. K. Sangwal, On the reverse indentation size effect and microhardness measurement of solids. *Mater. Chem. Phys.* **63**, 145–152 (2000). doi:10.1016/S0254-0584(99)00216-3
65. J. Gil Sevillano, H. Mughrabi, *Plastic Deformation and Fracture of Materials*. (VCH Verlagsges, Weinheim, 1993)
66. Meyer, Some Aspects of the Hardness of the Metals, Ph.D thesis, draft (1951)
67. K. Sangwal, A. Klos, Study of micro indentation hardness of different planes of gadmium calcium oxyborate single crystals. *Cryst. Res. Technol.* **40**, 429–438 (2005). doi:10.1002/crat.200410362
68. E.M. Onitsch, Über die Mikroharthe der Metalle. *Microskopie* **2**, 131–151 (1947)
69. W.A. Wooster, Physical properties and atomic arrangements in crystals. *Rep. Prog. Phys.* **16**, 62–82 (1953). doi:10.1088/0034-4885/16/1/302
70. O. Ozturk, T. Gokcen, S. Cavdar, H. Koralay, A.T. Tasci, A study on nucleation, crystallization kinetics, microstructure and mechanical properties of Ru–Bi partial substituted BSCCO glass ceramics. *J. Therm. Anal. Calorim.* **123**, 1073–1082 (2016). doi:10.1007/s10973-015-5028-8
71. G. Liu, J. Liu, X. Zheng, Y. Liu, D. Yuan, X. Zhang, Z. Gao, X. Tao, Bulk crystal growth and characterization of semi-organic non-linear optical crystal tri-ethylammonium hexachlorobismuthate (TDCB). *CrystEngComm.* **17**, 2569–2574 (2015). doi:10.1039/c4ce02182g
72. C.B. Proton, R.D. Rawling, Dependence of the Vickers indentation fracture toughness on the surface crack length. *Br. Ceram. Trans. J.* **88**, 83–90 (1989)
73. K. Nihara, R. Morena, D.P.H. Hasselman, Evaluation of  $K_{Ic}$  of brittle solids by the indentation method with low crack-to-indent ratios. *J. Mater. Sci. Lett.* **1**, 13–16 (1982). doi:10.1007/BF00724706
74. K. Jagannathan, S. Kalainathan, T. Gnanasekaran, Microhardness studies on 4-dimethyl amino-N-methyl 4-stilbazolium tosylate (DAST). *Mater. Lett.* **61**, 4485–4488 (2007). doi:10.1016/j.matlet.2007.02.033